Quasicrystalline electronic states in 30° rotated twisted bilayer graphene

Pilkyung Moon,[1,2,3,*] Mikito Koshino,[4] and Young-Woo Son[5]

[1]*Arts and Sciences, NYU Shanghai, Shanghai 200122, China; NYU-ECNU Institute of Physics at NYU Shanghai, Shanghai 200062, China*

[2]*Department of Physics, New York University, New York, New York 10003, USA*

[3]*State Key Laboratory of Precision Spectroscopy, East China Normal University, Shanghai 200062, China*

[4]*Department of Physics, Osaka University, Toyonaka, Osaka 560-0043, Japan*

[5]*Korea Institute for Advanced Study, Seoul 02455, Korea*

(Received 15 January 2019; published 29 April 2019)

The recently realized bilayer graphene system with a twist angle of 30° offers a new type of quasicrystal which unites the dodecagonal quasicrystalline nature and graphene's relativistic properties. Here, we introduce a concise theoretical framework that fully respects both the dodecagonal rotational symmetry and the massless Dirac nature, to describe the electronic states of the system. We find that the electronic spectrum consists of resonant states labeled by 12-fold quantized angular momentum, together with the extended relativistic states. The resulting quasiband structure is composed of the nearly flat bands with spiky peaks in the density of states, where the wave functions exhibit characteristic patterns which fit to the fractal inflations of the quasicrystal tiling. We also demonstrate that the 12-fold resonant states appear as spatially localized states in a finite-size geometry, which is another hallmark of quasicrystal. The theoretical method introduced here is applicable to a broad class of "extrinsic quasicrystals" composed of a pair of two-dimensional crystals overlaid on top of the other with incommensurate configurations.

DOI: 10.1103/PhysRevB.99.165430

I. INTRODUCTION

When two graphene layers are overlapped on top of the other, the interlayer twist angle θ is an important physical quantity to determine the electronic structures. This twisted bilayer graphene (TBG) is essentially a quasiperiodic system, as the two lattice periods of individual graphene layers are generally irrational to each other. When θ is relatively small (less than about 10°), however, the low-energy physics is governed by the long-range moiré interference pattern, and then the electronic properties are captured by the moiré effective theory that does not need an exact lattice matching. In brief, the effective theory approximately treats TBG as a translationally symmetric system ruled by the moiré period. The exotic phenomena in the low-angle regime [1,2], such as the flat band formation [3–9] and the Hofstadter butterfly under magnetic field [8,10–13], can be understood in terms of the moiré effective theory.

In TBG of large θ, on the other hand, the moiré period competes with the atomic length scale and the quasiperiodic nature emerges [14]. When $\theta = 30°$, in particular, the overlaid two hexagonal lattices are mapped onto a 12-fold rotationally symmetric quasicrystalline lattice without any translational symmetry [Fig. 1(a)], as first shown by Stampfli [15]. Recently, the TBG with a precise rotation angle of 30° was experimentally realized and its spectrum measured in epitaxially grown samples on top of the SiC surface [16]. In addition, similar TBGs have been realized on top of the Ni surface [17,18] and also by a transfer method [19]. Moreover, another 30°-rotated stack of atomic layers has also been realized in graphene on top of the BN layer [20] as well as the $MoSe_2$ bilayer system [21]. In such quasicrystalline TBG (QC-TBG), the moiré effective approach sketched above breaks down because its main assumption that the moiré pattern governs the system is no longer valid.

In the literature, several theoretical approaches have been applied to understand the electronic structures of conventional quasiperiodic systems [22], such as one-dimensional Fibonacci lattices [23,24], two-dimensional nonperiodic tiling including Penrose lattice [25,26], metal nanoparticles [27], photonic quasicrystals [28], and three-dimensional alloys including Al-Mn, Al-Ni-Co, and Al-Cu-Co [29–34]. These systems can be viewed as *intrinsic* quasicrystals where the atomic sites are intrinsically arranged in the quasiperiodic order. In contrast, the QC-TBG is regarded as an *extrinsic* quasicrystal, in that it is composed of a pair of perfect crystals having independent periodicities, and the quasiperiodic nature appears only in the perturbational coupling between the two subsystems. Thus, the QC-TBG unites the quasicrystalline order and the relativistic nature of the massless Dirac particles of graphene, yet it is not obvious whether and in what form the essential features of quasicrystals emerge in the electronic properties. Since such a hybrid situation is out of the scope of the previous theories of intrinsic quasicrystals, we need an alternative theoretical framework to properly describe the quasicrystalline physics of QC-TBG.

In this paper, we develop a concise model Hamiltonian that fully respects both the dodecagonal rotational symmetry and the massless Dirac nature to describe the quasicrystalline electronic states in the QC-TBG. We find that the electronic spectrum of QC-TBG is characterized by the 12-fold resonant states of relativistic Dirac fermions, and they can be well captured by a ring Hamiltonian composed of 12 Dirac cones.

*Corresponding author: pilkyung.moon@nyu.edu

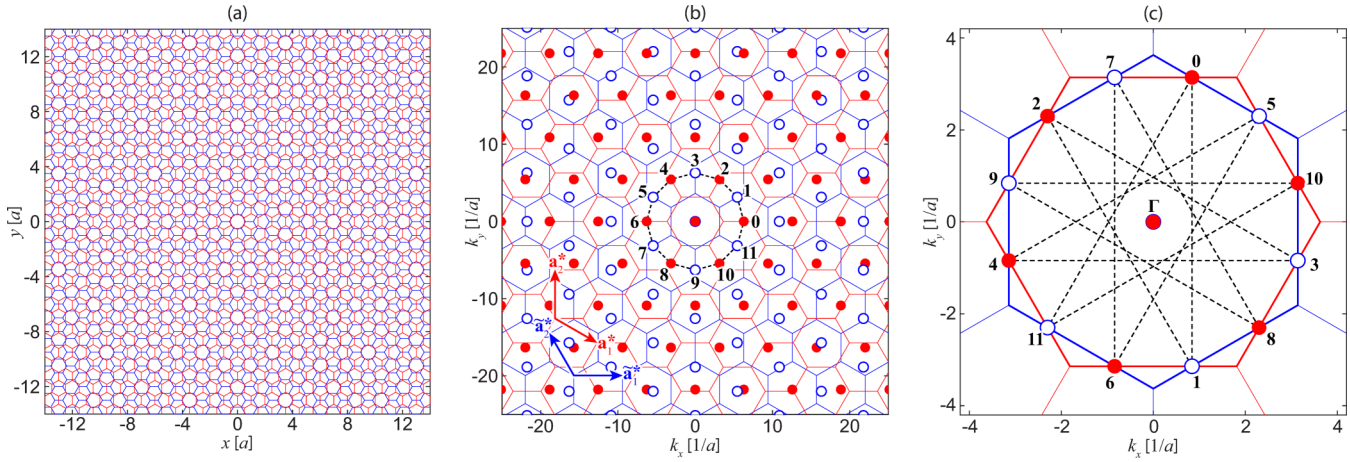

FIG. 1. (a) Real-space lattice structures of QC-TBG (TBG stacked at 30°). Red and blue hexagons represent the graphene's honeycomb lattices of layers 1 and 2, respectively. (b) Dual tight-binding lattice in the momentum space for QT-TBG (see text). Red and blue hexagons show the extended Brillouin zones of layers 1 and 2, respectively. The red filled circles represent the wave numbers $\mathbf{k}$ for layer 1, and blue open ones represent the inverted wave numbers $\mathbf{k}_0 - \tilde{\mathbf{k}}$ for layer 2, where $\mathbf{k}_0$ is taken as $\mathbf{0}$ here. The number n represents the position of $\mathbf{Q}_n$ ($n = 0, 1, 2, \ldots, 11$), and the dashed line indicates the connection in the 12-ring effective Hamiltonian. (c) The original positions of $\mathbf{k}$ (layer 1) and $\tilde{\mathbf{k}}$ (layer 2) associated with $\mathbf{Q}_n$, in the first Brillouin zone. The dashed line indicates the connection in the 12-ring Hamiltonian as in (a). Due to the symmetry, these 12 wave numbers are at the same distance from the Dirac point so that the intrinsic graphene's Bloch states at these wave numbers are all degenerate in energy.

The resulting quasiband structure comprises a series of the nearly flat bands corresponding to the resonant states, each of which is labeled by a 12-fold quantized angular momentum. The spatial pattern of wave functions exhibits the fractal inflations of the Stampfli tiling, which is a direct manifestation of the quasicrystalline nature [35]. Since we can tune the twist angles in the model, the transition of electronic states from the approximants [36] of QC-TBG to a true dodecagonal rotational symmetry can be continuously described within a 12-fold ring model, and the emergence of quasicrystalline states and the validity of the approximant method are critically attested. We also show that the 12-fold resonant states appear as spatially localized states in a finite-size geometry, which is another hallmark of the quasicrystalline nature [23,24,37]. The proposed theoretical approach is applicable to a broad class of extrinsic quasicrystals, and its simple structure of the closed Hamiltonian allows rigorous analysis on exotic quantum phenomena of quasicrystals.

The paper is organized as follows. In Sec. II, we present the tight-binding model for QC-TBG, and introduce the dual tight-binding approach in the momentum space. In Sec. III A, we derive the approximate 12-wave ring Hamiltonian and, using this, we describe the quasiband structure, the resonant states, and the characteristic wave functions to respect the Stampfli tiling. In Sec. III C, we calculate the electronic states of QC-TBG in an alternative method using the finite-size tight-binding model, and demonstrate the localization nature of the 12-fold resonant states. A brief conclusion is given in Sec. IV.

II. THEORETICAL METHODS

A. Tight-binding Hamiltonian for QC-TBG

We define the atomic structure of QC-TBG by starting from AA-stacked bilayer graphene (i.e., perfectly overlapping honeycomb lattices) and rotating the layer 2 around the center of hexagon by 30° [Fig. 1(a)]. We set xy coordinates parallel to the graphene layers and z axis perpendicular to the plane. The system belongs to the symmetry group D_{6d}, and it is invariant under an improper rotation $R(\pi/6)M_z$, where $R(\theta)$ is the rotation by an angle θ around the z axis, and M_z is the mirror reflection with respect to the xy plane. The primitive lattice vectors of layer 1 are taken as $\mathbf{a}_1 = a(1, 0)$ and $\mathbf{a}_2 = a(1/2, \sqrt{3}/2)$ with the lattice constant $a \approx 0.246$ nm, and those of the layer 2 as $\tilde{\mathbf{a}}_i = R(\pi/6)\,\mathbf{a}_i$. Accordingly, the reciprocal lattice vectors of layer 1 are given by $\mathbf{a}_1^* = (2\pi/a)(1, -1/\sqrt{3})$ and $\mathbf{a}_2^* = (2\pi/a)(0, 2/\sqrt{3})$, and layer 2 by $\tilde{\mathbf{a}}_i^* = R(\pi/6)\,\mathbf{a}_i^*$. The atomic positions are given by

$$\begin{aligned} \mathbf{R}_X &= n_1\mathbf{a}_1 + n_2\mathbf{a}_2 + \boldsymbol{\tau}_X \qquad \text{(layer 1)}, \\ \mathbf{R}_{\tilde{X}} &= \tilde{n}_1\tilde{\mathbf{a}}_1 + \tilde{n}_2\tilde{\mathbf{a}}_2 + \boldsymbol{\tau}_{\tilde{X}} \qquad \text{(layer 2)}, \end{aligned} \tag{1}$$

where n_i and $\tilde{n}_i$ are integers, $X = A, B$ ($\tilde{X} = \tilde{A}, \tilde{B}$) denotes the sublattice site of layer 1 (2), and $\boldsymbol{\tau}_X$ and $\boldsymbol{\tau}_{\tilde{X}}$ are the sublattice positions in the unit cell, defined by $\boldsymbol{\tau}_A = -\boldsymbol{\tau}_1$, $\boldsymbol{\tau}_B = \boldsymbol{\tau}_1$, $\boldsymbol{\tau}_{\tilde{A}} = -R(\pi/6)\boldsymbol{\tau}_1 + d\mathbf{e}_z$, $\boldsymbol{\tau}_{\tilde{B}} = R(\pi/6)\boldsymbol{\tau}_1 + d\mathbf{e}_z$ with $\boldsymbol{\tau}_1 = (0, a/\sqrt{3})$. Here, $d \approx 0.335$ nm is the interlayer spacing between graphene layers and $\mathbf{e}_z$ is the unit vector normal to the layer.

We model graphene by the tight-binding model of carbon p_z orbitals. The Hamiltonian is spanned by the Bloch bases of p_z orbitals at difference sublattices,

$$\begin{aligned} |\mathbf{k}, X\rangle &= \frac{1}{\sqrt{N}} \sum_{\mathbf{R}_X} e^{i\mathbf{k}\cdot\mathbf{R}_X} |\mathbf{R}_X\rangle \quad \text{(layer 1)}, \\ |\tilde{\mathbf{k}}, \tilde{X}\rangle &= \frac{1}{\sqrt{N}} \sum_{\mathbf{R}_{\tilde{X}}} e^{i\tilde{\mathbf{k}}\cdot\mathbf{R}_{\tilde{X}}} |\mathbf{R}_{\tilde{X}}\rangle \quad \text{(layer 2)}, \end{aligned} \tag{2}$$

where $|\mathbf{R}_X\rangle$ is the atomic p_z orbital at the site $\mathbf{R}_X$, $\mathbf{k}$ and $\tilde{\mathbf{k}}$ are the two-dimensional Bloch wave vectors, and $N = S/S_{\rm tot}$ is the number of graphene's unit cells $S = (\sqrt{3}/2)a^2$ in the total system area $S_{\rm tot}$. We assume that the transfer integral between any two p_z orbitals is expressed as [38]

$$-T(\mathbf{R}) = V_{pp\pi}\left[1-\left(\frac{\mathbf{R}\cdot\mathbf{e}_z}{R}\right)^2\right] + V_{pp\sigma}\left(\frac{\mathbf{R}\cdot\mathbf{e}_z}{R}\right)^2,$$
$$V_{pp\pi} = V^0_{pp\pi}e^{-(R-a/\sqrt{3})/r_0}, \quad V_{pp\sigma} = V^0_{pp\sigma}e^{-(R-d)/r_0}, \tag{3}$$

where $\mathbf{R}$ is the relative vector between two atoms, $V^0_{pp\pi} \approx -2.7$ eV, $V^0_{pp\sigma} \approx 0.48$ eV, and $r_0 \approx 0.0453$ nm [4,39].

The total tight-binding Hamiltonian is expressed as $H = H_1 + H_2 + U$ where H_1 and H_2 are the Hamiltonians for the intrinsic monolayer graphenes of layers 1 and 2, respectively, and U is for the interlayer coupling. The intralayer matrix elements of layer 1 are given by

$$\langle \mathbf{k}', X'|H_1|\mathbf{k}, X\rangle = h_{X,X'}(\mathbf{k})\delta_{\mathbf{k}',\mathbf{k}},$$
$$h_{X,X'}(\mathbf{k}) = \sum_{\mathbf{L}} -T(\mathbf{L}+\boldsymbol{\tau}_{X'X})e^{-i\mathbf{k}\cdot(\mathbf{L}+\boldsymbol{\tau}_{X'X})}, \tag{4}$$

where $\mathbf{L} = n_1\mathbf{a}_1 + n_2\mathbf{a}_2$ and $\boldsymbol{\tau}_{X'X} = \boldsymbol{\tau}_{X'} - \boldsymbol{\tau}_X$. Similarly, the matrix for H_2 is given by replacing $\mathbf{k}$ with $R(-\pi/6)\mathbf{k}$.

The interlayer matrix element between layers 1 and 2 is written as [1,7,40]

$$\langle \tilde{\mathbf{k}}, \tilde{X}|U|\mathbf{k}, X\rangle = -\sum_{\mathbf{G},\tilde{\mathbf{G}}} t(\mathbf{k}+\mathbf{G})e^{-i\mathbf{G}\cdot\boldsymbol{\tau}_X + i\tilde{\mathbf{G}}\cdot\boldsymbol{\tau}_{\tilde{X}}}\,\delta_{\mathbf{k}+\mathbf{G},\tilde{\mathbf{k}}+\tilde{\mathbf{G}}}, \tag{5}$$

where $\mathbf{G} = m_1\mathbf{a}^*_1 + m_2\mathbf{a}^*_2$ and $\tilde{\mathbf{G}} = \tilde{m}_1\tilde{\mathbf{a}}^*_1 + \tilde{m}_2\tilde{\mathbf{a}}^*_2$ ($m_1, m_2, \tilde{m}_1, \tilde{m}_2 \in \mathbb{Z}$) run over all the reciprocal points of layers 1 and 2, respectively. We also defined

$$t(\mathbf{q}) = \frac{1}{S}\int T(\mathbf{r} + z_{\tilde{X}X}\mathbf{e}_z)e^{-i\mathbf{q}\cdot\mathbf{r}}d\mathbf{r}, \tag{6}$$

where $z_{\tilde{X}X} = (\boldsymbol{\tau}_{\tilde{X}} - \boldsymbol{\tau}_X)\cdot\mathbf{e}_z$.

B. Dual tight-binding lattice in momentum space

Equation (5) shows that the interlayer interaction occurs between the states satisfying the generalized umklapp scattering condition $\mathbf{k}+\mathbf{G} = \tilde{\mathbf{k}}+\tilde{\mathbf{G}}$. When we start from the layer 1's Bloch states at $\mathbf{k}_0$, for example, the interlayer Hamiltonian U couples this state with layer 2's Bloch states at $\tilde{\mathbf{k}} = \mathbf{k}_0 + \mathbf{G} - \tilde{\mathbf{G}}$. They are further coupled back to layer 1's states at $\mathbf{k} = \mathbf{k}_0 + \mathbf{G}' - \tilde{\mathbf{G}}'$, and so forth. As a result, the space of the wave functions associated with $\mathbf{k}_0$ is spanned by $\{|\mathbf{k}, X\rangle \,|\, \mathbf{k} = \mathbf{k}_0 + \tilde{\mathbf{G}} - \mathbf{G}\}$ and $\{|\tilde{\mathbf{k}}, \tilde{X}\rangle \,|\, \tilde{\mathbf{k}} = \mathbf{k}_0 + \mathbf{G} - \tilde{\mathbf{G}}\}$ for $\forall\,\mathbf{G}$ and $\forall\,\tilde{\mathbf{G}}$. However, we actually need only a subset of these sets since the Brillouin zone (BZ) of each layer is translationally invariant with respect to the reciprocal lattice vectors of its own (i.e., $\mathbf{k}$ and $\mathbf{k}+\mathbf{G}$ stand for the same Bloch wave number of layer 1). Thus, without loss of generality, we can choose the subspace spanned by the QC-TBG Hamiltonian as $\{|\mathbf{k}, X\rangle \,|\, \mathbf{k} = \mathbf{k}_0 + \tilde{\mathbf{G}},\ \forall\,\tilde{\mathbf{G}}\}$ and $\{|\tilde{\mathbf{k}}, \tilde{X}\rangle \,|\, \tilde{\mathbf{k}} = \mathbf{k}_0 + \mathbf{G},\ \forall\,\mathbf{G}\}$. Here, note that the k points in each layer is regularly spaced with the reciprocal vectors of the other layer.

According to Eq. (5), the interaction strength between $\mathbf{k} = \mathbf{k}_0 + \tilde{\mathbf{G}}$ and $\tilde{\mathbf{k}} = \mathbf{k}_0 + \mathbf{G}$ is given by $t(\mathbf{q})$ where $\mathbf{q} = \mathbf{k}+\mathbf{G} = \tilde{\mathbf{k}}+\tilde{\mathbf{G}} = \mathbf{k}+\tilde{\mathbf{k}}-\mathbf{k}_0$. Since $t(\mathbf{q})$ decays in large $\mathbf{q}$, the relevant contribution occurs only when $|\mathbf{k}+\tilde{\mathbf{k}}-\mathbf{k}_0|$ is relatively small. The interaction strength can be visualized by the diagram Fig. 1(b), where all the layer 2's wave points $\tilde{\mathbf{k}}$ are inverted to $\mathbf{k}_0 - \tilde{\mathbf{k}}$, and overlapped with the layer 1's wave points $\mathbf{k}$. In the map, the quantity $|\mathbf{k}+\tilde{\mathbf{k}}-\mathbf{k}_0|$ is the geometrical distance given by two points, so that the interaction takes place only between the points located in close distance. If the k points are viewed as "sites," the whole system can be recognized as a tight-binding lattice in k space, which is the dual counterpart of the original tight-binding Hamiltonian in the real space. It should be noted that, unlike the real-space version, the intralayer Hamiltonians H_1 and H_2 now can be interpreted as k-dependent onsite potential in the k space, which is nothing but the band energy of intrinsic graphene. Recently, the relationship between the real space and the momentum space was also noticed in the localized wave functions in moiré bilayer systems [41].

In this k-space tight-binding model, the hopping between different k-space sites (the interlayer interaction U) is smaller by an order of magnitude than the potential landscape (the band energy), so that the eigenfunctions tend to be localized in the k-space lattice, in a similar manner to the Aubry-André model in one dimension [42]. In the practical calculation, therefore, we are allowed to take only a limited number of wave points around $\mathbf{k}_0$ inside a certain cutoff circle, and obtain the energy eigenvalues by diagonalizing the Hamiltonian matrix within the finite bases. If we plot the energy levels against $\mathbf{k}_0$, we obtain the quasiband structures of the system. Here the wave number $\mathbf{k}_0$ works like the crystal momentum for the periodic system, so it can be called the quasicrystal momentum. The cutoff radius k_c should be greater than the typical localization length in the k space, but need not be too large since the wave points discarded outside k_c are properly considered by shifting $\mathbf{k}_0$. If we increase k_c, we will see more and more replicas of the identical quasienergy band with different origins because shifting $\mathbf{k}_0$ actually corresponds to taking a different origin in the k-space map of Fig. 1(b). The resonant band structure near $\mathbf{k}_0 = 0$ barely changes in this process because its wave function is very well localized to the 12-membered ring in the k space. The replica bands are just a duplication of the same states so they should be appropriately removed in calculating the physical quantities such as the density of states. The validity of the momentum cutoff is discussed in detail in Appendix A.

III. RESULTS AND DISCUSSION

A. 12-fold symmetric resonant states

At $\mathbf{k}_0 = \mathbf{0}$, we see that the 12 symmetric points $\mathbf{Q}_n = a^*[\cos(n\pi/6), \sin(n\pi/6)]$ ($n = 0, 1, 2, \ldots, 11$) form a circular chain in the dual-tight-binding lattice of which radius is $a^* \equiv |\mathbf{a}^*_i| = 4\pi/(\sqrt{3}a)$, indicated by the dashed ring in Fig. 1(b). Noting that the layer 2's wave points are inverted, these points are associated with layer 1's Bloch wave numbers $\mathbf{k} = \mathbf{Q}_n$ for even n's and layer 2's $\tilde{\mathbf{k}} = -\mathbf{Q}_n$ for odd n's. Figure 1(c) shows the original positions of $\mathbf{k}$ (layer 1) and $\tilde{\mathbf{k}}$

(layer 2) associated with $\mathbf{Q}_n$, in the first Brillouin zone. Due to the symmetry, the intrinsic graphene's Bloch states at the 12 points are all degenerate in energy, and therefore the interlayer coupling hybridizes them to make resonant states. Here, the coupling is only relevant between the neighboring sites of the ring, and it is given by $t_0 = t(2a^* \sin 15^\circ) \approx 157$ meV.

In the vicinity of $\mathbf{k}_0 = \mathbf{0}$, the Hamiltonian of the ring can be expressed by a 24×24 matrix

$$\mathcal{H}_{\rm ring}(\mathbf{k}_0) = \begin{pmatrix} H^{(0)} & W^\dagger & & & & W \\ W & H^{(1)} & W^\dagger & & & \\ & W & H^{(2)} & W^\dagger & & \\ & & \ddots & \ddots & \ddots & \\ & & & W & H^{(10)} & W^\dagger \\ W^\dagger & & & & W & H^{(11)} \end{pmatrix}, \tag{7}$$

$$H^{(n)}(\mathbf{k}_0) = \begin{pmatrix} h^{(n)}_{AA} & h^{(n)}_{AB} \\ h^{(n)}_{BA} & h^{(n)}_{BB} \end{pmatrix}, \quad W = -t_0 \begin{pmatrix} \omega & 1 \\ 1 & \omega^* \end{pmatrix}, \tag{8}$$

where $h^{(n)}_{X'X}(\mathbf{k}_0) = h_{X'X}[R(-7n\pi/6)\mathbf{k}_0 + \mathbf{Q}_0]$, $\omega = e^{2\pi i/3}$, and we neglect the $\mathbf{k}_0$ dependence of the interlayer matrix element $t(\mathbf{q})$. The diagonal block $H^{(n)}$ represents the monolayer's Hamiltonian at $\mathbf{k} = \mathbf{k}_0 + \mathbf{Q}_n$ for even n (layer 1) and $\tilde{\mathbf{k}} = \mathbf{k}_0 - \mathbf{Q}_n$ for odd n (layer 2). In each 2×2 block the sublattices are arranged in the order of (A, B) or $(\tilde{A}, \tilde{B})$ for $n \equiv 0, 3$ in modulo of 4, and (B, A) or $(\tilde{B}, \tilde{A})$ for $n \equiv 1, 2$. By doing this, the first base of a 2×2 block is always mapped to the first base of other block under the operation of $R(\pi/6)M_z$. Note that the arrangement of h_{AA}, h_{AB}, etc., in the submatrix $H^{(n)}$ is fixed irrespective of n, and the dependence on n solely comes from $R(-7n\pi/6)\mathbf{k}_0$ in the argument of $h_{X'X}$. Consequently, the total Hamiltonian $\mathcal{H}_{\rm ring}$ is obviously symmetric under rotation by a single span of the ring (i.e., moving $\mathbf{Q}_n$ to $\mathbf{Q}_{n+1}$), which actually corresponds to the operation $[R(\pi/6)M_z]^7$ (210° rotation and swapping layers 1 and 2) in the original system.

Figure 2(a) shows the density of states (DOS), Fig. 2(b) the band structures as a function of $\mathbf{k_0}$ in the negative energy region, and Fig. 2(c) its closer view near $\mathbf{k}_0 = \mathbf{0}$. The 12 Dirac cones are arranged on a circle with a radius $\Delta k = 4(2 - \sqrt{3})\pi/(3a)$ and they are strongly mixed near $\mathbf{k}_0 = \mathbf{0}$. As a result, the originally degenerate 12 states of graphene (in each of the electron side and the hole side of the Dirac cone) split into different energies, and exhibit the characteristic dispersion including flat band bottoms and the Mexican-hat edges. This leads to a series of spiky peaks and dips (pseudogaps) in DOS. At $\mathbf{k}_0 = \mathbf{0}$, the Hamiltonian can be analytically diagonalized to obtain a set of energies (neglecting the constant energy)

$$E^{\pm}_m = t_0 \cos q_m \pm \sqrt{3t_0^2 \sin^2 q_m + (h_0 - 2t_0 \cos q_m)^2}, \tag{9}$$

where $h_0 = h_{AB}(\mathbf{Q}_0) = h_{BA}(\mathbf{Q}_0) = 1.84$ eV, $\pm$ corresponds to the conduction band and valence band, respectively, and $q_m = (7\pi/6)m$ with $m = -5, -4, \ldots, 5, 6$ is the wave number along the chain. The eigenvalue of $R(\pi/6)M_z$ is given by $e^{im\pi/6}$. Here, the states with $m = \pm s$ $(s = 1, 2, 3, 4, 5)$ form twofold doublets, and belong to two-dimensional E_s irreducible representation of D_{6d} point group. The $m = 0$ and 6 are nondegenerate, and belong to A_1 (A_2) and B_2 (B_1), respectively, for the conduction (valence) band. If we disregard the z-position difference, the index m is regarded as quantized angular momentum in 12-fold rotational symmetry, and this is an essential characteristics of quasicrystal TBG.

We have similar resonant states also in the conduction band, while the energy scale of the band structures is much smaller than in the valence band. Equation (9) clearly explains such asymmetry; the dispersion of E^-_m in q_m is nearly three times wider than that of E^+_m, considering that $h_0 \gg t_0$. Intuitively, the wave function of the conduction band of intrinsic graphene has the opposite phases between the sublattices A and B, and then the interlayer coupling between incommensurate layers tends to be suppressed by the phase cancellation.

B. Wave functions showing the quasicrystal tiling

The 12-wave resonant coupling also gives rise to a characteristic pattern in the wave function. Figure 2(d) shows the wave functions at $\mathbf{k}_0 = \mathbf{0}$ where the hybridization is the most prominent, where we can see that the wave amplitude distributes selectively on a limited number of sites in a 12-fold rotationally symmetric pattern. The extent of the hybridization of different wave modes is characterized by the inverse participation ratio (IPR) on the dominant layer

$$P^{-1}(\psi) = \frac{\sum'_i |\psi_i|^4}{\left(\sum'_i |\psi_i|^2\right)^2}. \tag{10}$$

Here, ψ_i is the amplitude at the site i of the eigenstates ψ, and $\sum'_i$ represents the sum over the sites on the dominant layer, which is defined as the layer having greater wave amplitude than the other. We have $P^{-1} = 1$ for a pure single-layer state, and $P^{-1} = 1.5$ for a hybrid state of two plane wave modes. In Fig. 2(b), the blue dots represent IPR at several sample points in the band structures along the x direction, where the dot area is proportional to $P^{-1} - 1$. We see that the IPR becomes large exclusively around $\mathbf{k}_0 = \mathbf{0}$, where the 12 wave components are strongly hybridized. P^{-1} remains almost 1 near the Dirac cones where the hybridization is almost negligible. We also have a region of $P^{-1} \sim 1.5$ along the arch-shaped gap below the Dirac cone, which is indicated by "2-wave" in Fig. 3(b). These "2-wave" states arise from the hybridization of the K and K' of the *same* layer assisted by the second-order process of the interlayer coupling U.

We also show a large-scale plot of $m = 0, 6$ states in Fig. 3(a). We see that the wave pattern perfectly follows the Stampfli tiling, where the red (left-half) and black (right-half) lines represent the third and fourth generations of the fractal inflation, respectively [15]. Such a long-range structure of the quasicrystalline wave function is actually quite sensitive to a slight change of the twist angle. Figure 3(b) represents the wave pattern of the corresponding state in TBG with $\theta = 29.84^\circ$, calculated by the same 12-wave method. The TBG of 29.84° is a quasicrystal approximant, which is not quasiperiodic but has a translational symmetry with period of 3.31 nm. We can see that the local wave pattern is quite similar to that of 30°, while the long-range quasiperiodic nature is completely lost and round to a periodic pattern. Here, we confirmed that the quasiband structures, DOS, and

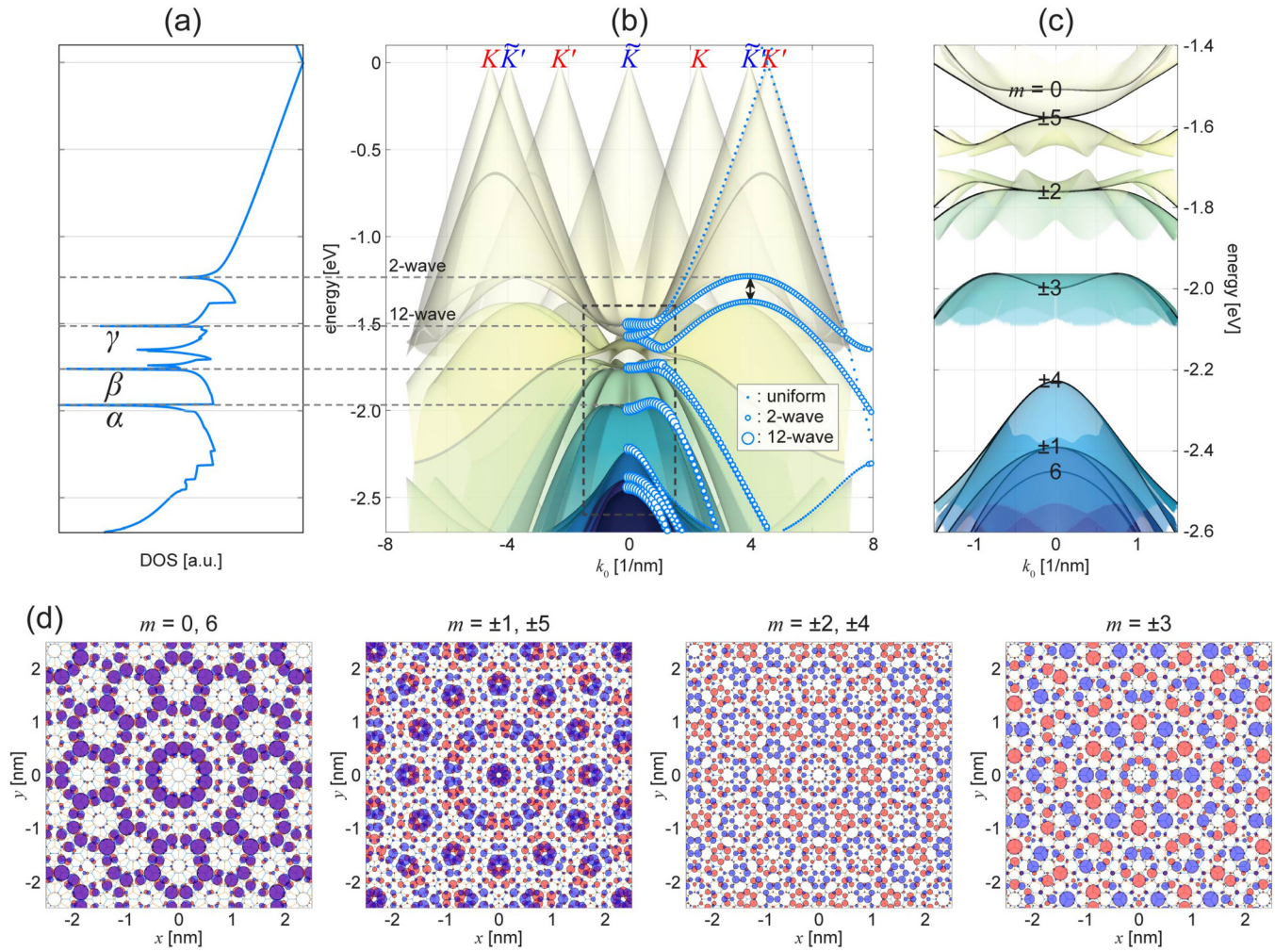

FIG. 2. (a) DOS and (b) electronic structures in the valence band side of QC-TBG calculated by the 12-ring effective model. Blue dots represent the inverse participation ratio of the dominant layer at several sample points in the band structures, where the dot area is proportional to the measure of the spatial extent of the wave functions. Inset shows the size of the dots for almost decoupled states ("uniform"), the states arise from the hybridization of the two waves in the same layer ("2-wave"), and the states arise from the hybridization of twelve waves ("12-wave") (see text). The black arrow shows the gap opening caused by 2-wave mixing. (c) Detailed band structures near $\mathbf{k} = \mathbf{0}$ with index m indicating quantized angular momentum in 12-fold rotational symmetry. (d) The valence band wave functions at $\mathbf{k} = \mathbf{0}$ characterized by m, where the area of the circle is proportional to the squared wave amplitude, and red and blue circles represent the states in the upper and the lower layers, respectively.

IPR look almost the same as 30°, but the tiny change of the wave bases and the coupling matrix elements in the 12-ring Hamiltonian encodes the periodic/quasiperiodic transition.

The energy spectrum of the QC-TBG approximant can also be calculated by the original real-space tight-binding model since it has a finite superlattice unit cell. We can show that the DOS and the wave function of 29.84° calculated by the original tight-binding model are virtually the same as the result of the 12-ring effective Hamiltonian, and this justifies the validity the effective approach. In Appendix B, we present an extensive study on the electronic structures of the quasiapproximants in all the angle regions from 0° to 30°.

C. Localization in finite-sized QC-TBG

The emergence of quasicrystalline states in QC-TBG can also be confirmed by a finite-sized tight-binding lattice, while the computation is enormous. Here, we consider a tight-binding lattice composed of two large disks of graphene with radius $R = 39.4$ nm stacked at exactly 30°, and calculate its electronic structures by diagonalizing the huge Hamiltonian matrix with the total number of atoms 371 532. As shown in Fig. 4(a), the DOS of the finite flakes (thick red line), which is obtained by broadening its discrete spectrum, is consistent with the DOS of the 12-wave effective model (thin black line) calculated by the effective Hamiltonian with a few wave bases [Fig. 2(b)]. In Fig. 4(b), we also present the wave functions at three energies α, β, and γ, which correspond to the band edges of the quasiband structures in the effective Hamiltonian (Fig. 2).

The magnified plot of γ is presented in the inset of Fig. 4(b) showing the characteristic pattern of 12-wave approximation. Interestingly, however, it is overlapped with an envelope function decaying in the radial direction. Such a localized feature

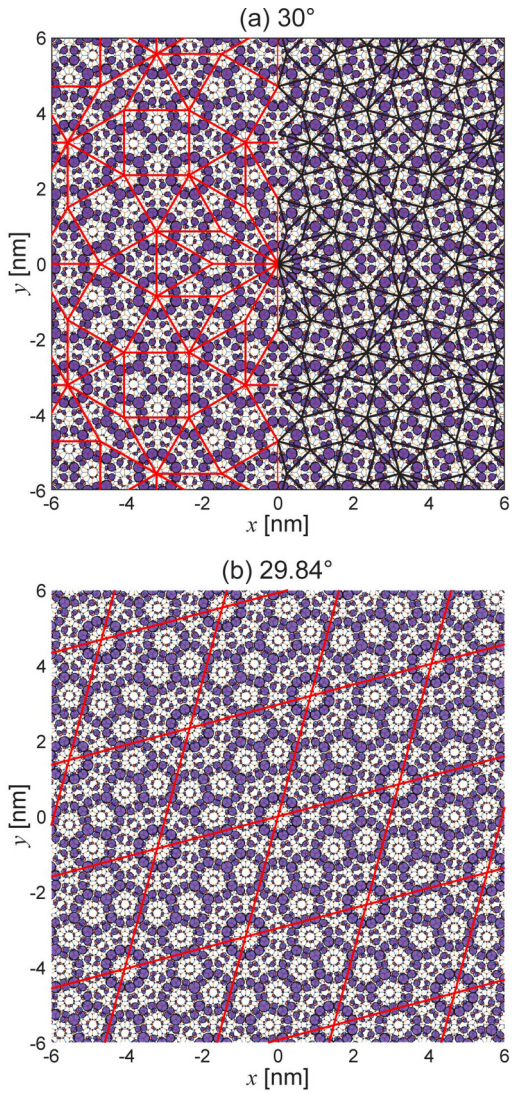

FIG. 3. (a) Large-scale plot of $m = 0, 6$ states of TBG with $\theta = 30^\circ$ in Fig. 2(d). Red (left-half) and black (right-half) lines represent the fourth and third generations of the Stampfli tiling, respectively. (b) Similar plot for the quasicrystal approximant with $\theta = 29.84^\circ$. The red lines indicate the periodic unit cell.

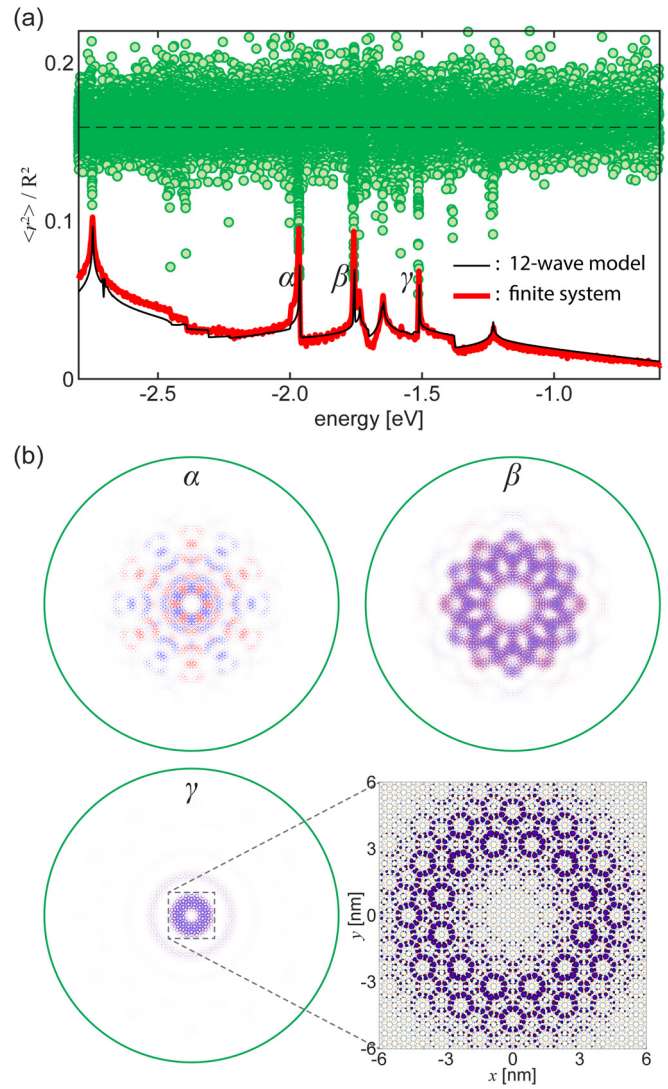

FIG. 4. (a) DOS (red line) and the generalized second momentum (green filled circles) of the two large finite flakes of graphene, with 371 532 atoms (radius of the flake ∼39.4 nm), stacked at exactly 30°. Black line shows the DOS of the k-space model [12-wave model ($k_c < 18.8/a$)]. (b) Plots similar to Fig. 2(d) for each peak α, β, γ.

is never seen in single-layer graphene and it is the characteristics of the resonant states of QC-TBG. As a measure of the concentration to the center, we calculate the second momentum $\langle r^2\rangle/R^2$ for each eigenstate and plot it as green circles in Fig. 4(a). For a uniform state (i.e., the wave amplitude is constant throughout the system), $\langle r^2\rangle/R^2$ approaches $1/(2\pi)$, which is indicated by the dashed line. We can actually see that $\langle r^2\rangle/R^2$ lies around this line for most of the states, while it becomes exceptionally small at the energies of the quasiband edges argued in the previous section. In terms of the quasiband structures, these localized states actually correspond to the integral of the quasiband states over the nearly flat region, and the length scale of the envelope function is related to the size of the flat area in the momentum space. For the state at γ ($m = 0$ state), for instance, the radius of the flat area is roughly given by $\delta k \sim 0.2/a$, and the corresponding real-space scale $r = 2\pi/k \sim 7.7$ nm matches the characteristic decaying and oscillating scale of the envelope function.

IV. CONCLUSIONS

We revealed that the quasicrystalline nature emerges in the electronic properties of QC-TBG, or the twisted bilayer graphene stacked at 30°. We developed a concise model Hamiltonian for this unique system, and demonstrated that the electronic structure is well described by the quasiband picture despite the lack of periodicity. The quasiband states of the QC-TBG are characterized by the 12-fold resonant states of relativistic Dirac fermions, where the wave functions exhibit the spatial pattern fully respecting the dodecagonal quasicrystal tiling. Such a nonuniform distribution of electron may be observed by microscopy imaging techniques. The emergence of quasicrystalline states was attested by comparing the QC-TBG and a periodic approximant near 30°, and it was demonstrated that even a slight deviation from the QC configuration destroys the long-range quasicrystalline

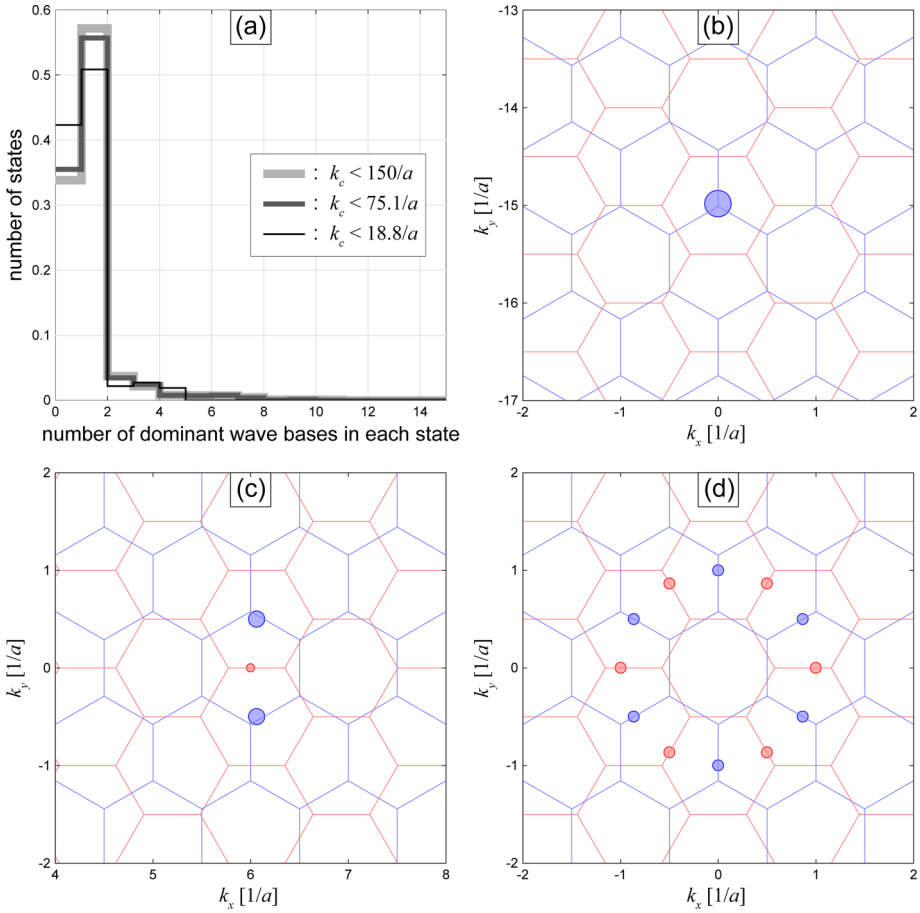

FIG. 5. (a) Histogram of the number of dominant wave base components $|\mathbf{k}, X\rangle$ and $|\tilde{\mathbf{k}}, X\rangle$ that make up each state. Thick light gray, middle dark gray, thin black lines show the histogram for all the states calculated with the wave bases within k_c of $150/a$, $75.1/a$, $18.8/a$, respectively, where the total number of wave bases are 11 630, 2918, 182, respectively. The histogram is normalized by the total number of states, which is two times the number of wave bases due to the sublattices. (b)–(d) The dominant component wave bases of three example states in the k space. The radius of each shaded red (blue) circles is proportional to the amplitude of each wave basis in layer 1 (2). (b) The wave component of a nearly decoupled, monolayerlike state. (c) The state which originates from the 2-wave mixing. And, (d) the 12-wave resonance state.

nature. Finally, we studied the electronic states of QC-TBG using the finite-size tight-binding model, where the 12-fold resonant states appear as spatially localized states in a finite-size geometry.

While we considered the QC-TBG as a model example in this paper, the theoretical method based on the k-space tight-binding approach introduced here is applicable to any kind of extrinsic quasicrystal composed two-dimensional materials overlaid in incommensurate configurations, including heterostructures of two-dimensional materials having difference lattice symmetries (e.g., rectangle and hexagon).

Extrinsic quasicrystals also provide a unique opportunity to tune the quasicrystal bands by controlling the interlayer interaction strength U. As U is an exponential function of the interlayer spacing d [43], we can either increase U by applying pressure, or decrease it through intercalation of ions or addition of barrier atomic layers [44]. When U becomes comparable to the width of the energy bands, we expect a transition from the weakly coupled regime to the strongly coupled regime where the quasicrystalline nature is even more pronounced. The detailed studies on exotic electronic natures in a broad class of extrinsic quasicrystals, such as the electronic transport, optical properties, the quantum Hall effect, and also the effects of U modulation to these phenomena, are left for future research.

ACKNOWLEDGMENTS

We thank L. A. Wray and A. Kent for fruitful discussions. P.M. was supported by NYU Shanghai (Start-Up Funds), NYU-ECNU Institute of Physics at NYU Shanghai, New York University Global Seed Grants for Collaborative Research. This research was carried out on the High Performance Computing resources at NYU Shanghai and CAC of KIAS. M.K. was supported by JSPS KAKENHI Grants No. JP25107005, No. JP15K21722, and No. JP17K05496. Y.-W.S. was supported by NRF of Korea (Grant No. 2017R1A5A1014862, SRC program: vdWMRC center).

P.M. and M.K. contributed equally to this work.

APPENDIX A: VALIDITY OF THE MOMENTUM-SPACE CUTOFF

In this Appendix, we argue about the validity of introducing the momentum-space cutoff in calculating the quasiband structure. As we mentioned in Sec. II B, the wave functions of the QC-TBG are localized in the k space in a similar manner to the Aubry-André model in one dimension [42] because the hopping term in the k space is much smaller than the potential landscape (the band energy). Figures 5(b)–5(d) show some examples of the k-space amplitude map. Figure 5(b) shows a nearly decoupled state which is dominated by only a single state of monolayer graphene, and Fig. 5(c) is a state originating from the 2-wave mixing, where a pair of monolayer's states on layer 2 are coupled though the mediation of a middle state on layer 1. Figure 5(d) is the 12-wave resonant state. Any eigenstates other than those examples are also localized within just a few reciprocal lattice constants in k space. When we increase the number of total wave base components

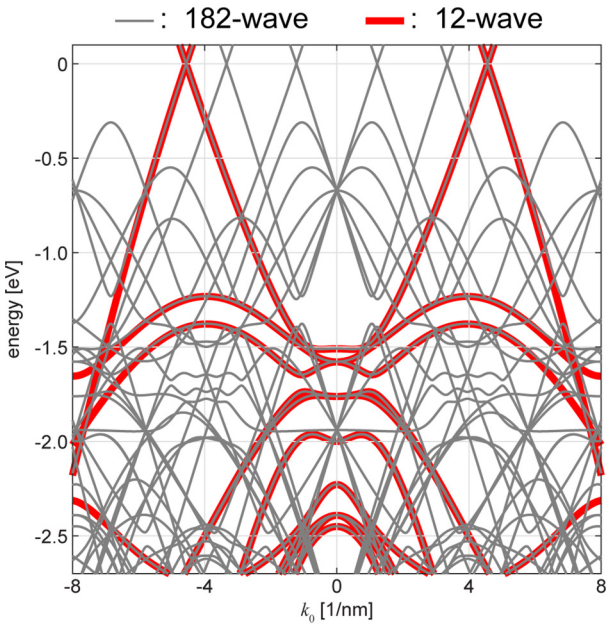

FIG. 6. Quasiband structure of QC-TBG calculated by 12-wave model (thin red lines) and 182-wave model (thick gray lines).

($|\mathbf{k}, X\rangle$ and $|\tilde{\mathbf{k}}, \tilde{X}\rangle$) by increasing k_c, each eigenstate hardly changes as long as k_c is greater than the typical localization length. In Fig. 5(a), we show the histogram of the number of dominant wave components in the eigenstates at a particular $\mathbf{k}_0$, calculated in the basis sets within k_c of $150/a$, $75.1/a$, and $18.8/a$, respectively, where the total number of wave bases are 11 630, 2918, and 182, respectively. We actually see that each of eigenstates is composed only a few (mostly less than 10) bases. We note that, in large k_c, we often see a resonance between different localized states which are very distant in k space. This does not much affect the calculation of the physical quantity because the overlap of the different localized wave functions are exponentially small.

We have infinitely many localized states far away from the first Brillouin zone, so one might think that it is necessary to take an infinite k_c to properly include all the states. Note that, however, these localized states can be moved into the vicinity of the first Brillouin zone by shifting $\mathbf{k}_0$ with a proper amount, as we show in the following. Thus, instead of using a large k_c requiring a large computational cost, we can obtain the full spectrum of the system by calculating the electronic structures as a function of $\mathbf{k}_0$ with a moderate k_c.

Let us consider two states $|\mathbf{k}_1, X\rangle$ and $|\tilde{\mathbf{k}}_1, \tilde{X}\rangle$ with

$$\begin{aligned} \mathbf{k}_1 &= \mathbf{k}_0 + \tilde{\mathbf{G}}_1 \quad (\tilde{\mathbf{G}}_1 \in \tilde{\mathbf{G}}), \\ \tilde{\mathbf{k}}_1 &= \mathbf{k}_0 + \mathbf{G}_1 \quad (\mathbf{G}_1 \in \mathbf{G}) \end{aligned} \tag{A1}$$

for a given $\mathbf{k}_0$. Suppose $\mathbf{k}_1$ and $\tilde{\mathbf{k}}_1$ are outside the cutoff circle, i.e., $|\mathbf{k}_1| > k_c$ and $|\tilde{\mathbf{k}}_1| > k_c$, but they strongly interact with each other, i.e.,

$$|\mathbf{q}(= \mathbf{k}_0 + \mathbf{G}_1 + \tilde{\mathbf{G}}_1)| \leqslant \mathcal{O}(|\mathbf{a}_i^*|). \tag{A2}$$

Now, for any such $\mathbf{k}_1$, we can always find $\mathbf{G}_2$ ($\mathbf{G}_2 \in \mathbf{G}$) which makes $\mathbf{k}_1$ move to the point $\mathbf{k}_2 \equiv \mathbf{k}_1 - \mathbf{G}_2$ in the first Brillouin zone, i.e.,

$$|\mathbf{k}_2| \leqslant \mathcal{O}(|\mathbf{a}_i^*|). \tag{A3}$$

And suppose $\tilde{\mathbf{k}}_2$, defined as

$$\tilde{\mathbf{k}}_2 \equiv \mathbf{k}_0 + \mathbf{G}_1 + \tilde{\mathbf{G}}_1. \tag{A4}$$

Then, by shifting $\mathbf{k}_0$ to a new point $\mathbf{k}_0'$ defined as

$$\mathbf{k}_0' \equiv \mathbf{k}_2, \tag{A5}$$

we can see that

$$\begin{aligned} \mathbf{k}_2 &= \mathbf{k}_0' + \mathbf{0} \quad (\mathbf{0} \in \tilde{\mathbf{G}}), \\ \tilde{\mathbf{k}}_2 &= \mathbf{k}_0' + \mathbf{G}_1 + \mathbf{G}_2 \quad (\mathbf{G}_1 + \mathbf{G}_2 \in \mathbf{G}) \end{aligned} \tag{A6}$$

are the member of the subspace spanned from $\mathbf{k}_0'$. And by considering that $\tilde{\mathbf{k}}_2 = \mathbf{q}$, and from Eqs. (A2) and (A3), we can show that these two points are within the cutoff circle. Since

$$\begin{aligned} \mathbf{k}_2(= \mathbf{k}_0 + \tilde{\mathbf{G}}_1 - \mathbf{G}_2) &= \mathbf{k}_1(= \mathbf{k}_0 + \tilde{\mathbf{G}}_1) \quad (\text{mod } \mathbf{G}), \\ \tilde{\mathbf{k}}_2(= \mathbf{k}_0 + \mathbf{G}_1 + \tilde{\mathbf{G}}_1) &= \tilde{\mathbf{k}}_1(= \mathbf{k}_0 + \mathbf{G}_1) \quad (\text{mod } \tilde{\mathbf{G}}), \end{aligned} \tag{A7}$$

$|\mathbf{k}_2, X\rangle$ and $|\tilde{\mathbf{k}}_2, \tilde{X}\rangle$ represent the Bloch states the same as $|\mathbf{k}_1, X\rangle$ and $|\tilde{\mathbf{k}}_1, \tilde{X}\rangle$, respectively, interacting with the same interaction strength $t(\mathbf{q})$, since

$$\mathbf{q}' \equiv \mathbf{k}_2 - (\mathbf{k}_0' - \tilde{\mathbf{k}}_2) = \mathbf{q}. \tag{A8}$$

Thus, by shifting $\mathbf{k}_0$ to $\mathbf{k}_0'$, the points discarded outside k_c with $\mathbf{k}_0$ are properly considered. And by calculating the electronic structures for every $\mathbf{k}_0$ in the first Brillouin zone, we can get every possible interaction pair in this system.

Figure 6 shows the quasicrystal bands of QC-TBG calculated with 12-wave model ($k_c < 3.76/a$ with $\mathbf{k} = \mathbf{0}$ removed) and 182-wave model ($k_c < 18.8/a$). We can see that the band structure of 182-wave model fully includes the spectrum of 12-wave model, while it also contains many other band lines. Actually, these extra lines are just replicas of the identical quasicrystal bands of 12-wave model with different origins (Sec. II B). In other words, the physical properties can be well described by calculating the quasiband structure with a relatively short k_c.

The minimum 12-wave models well reproduce the band structure near the 12-wave resonant states, while there are

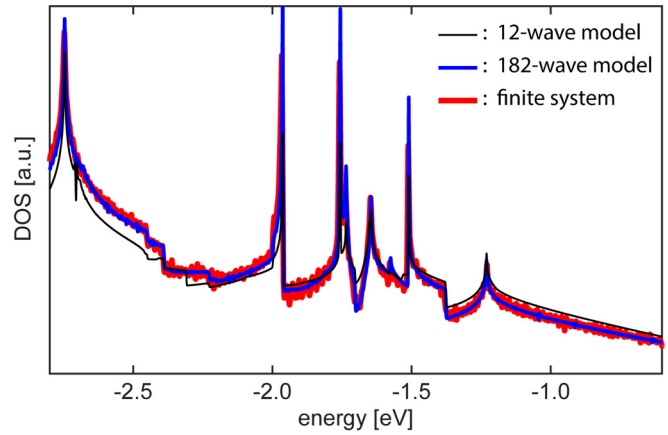

FIG. 7. DOS of QC-TBG calculated by 12-wave bases (thin black line) and 182-wave bases (middle blue line). The thick red line shows the DOS of finite-sized QC-TBG.

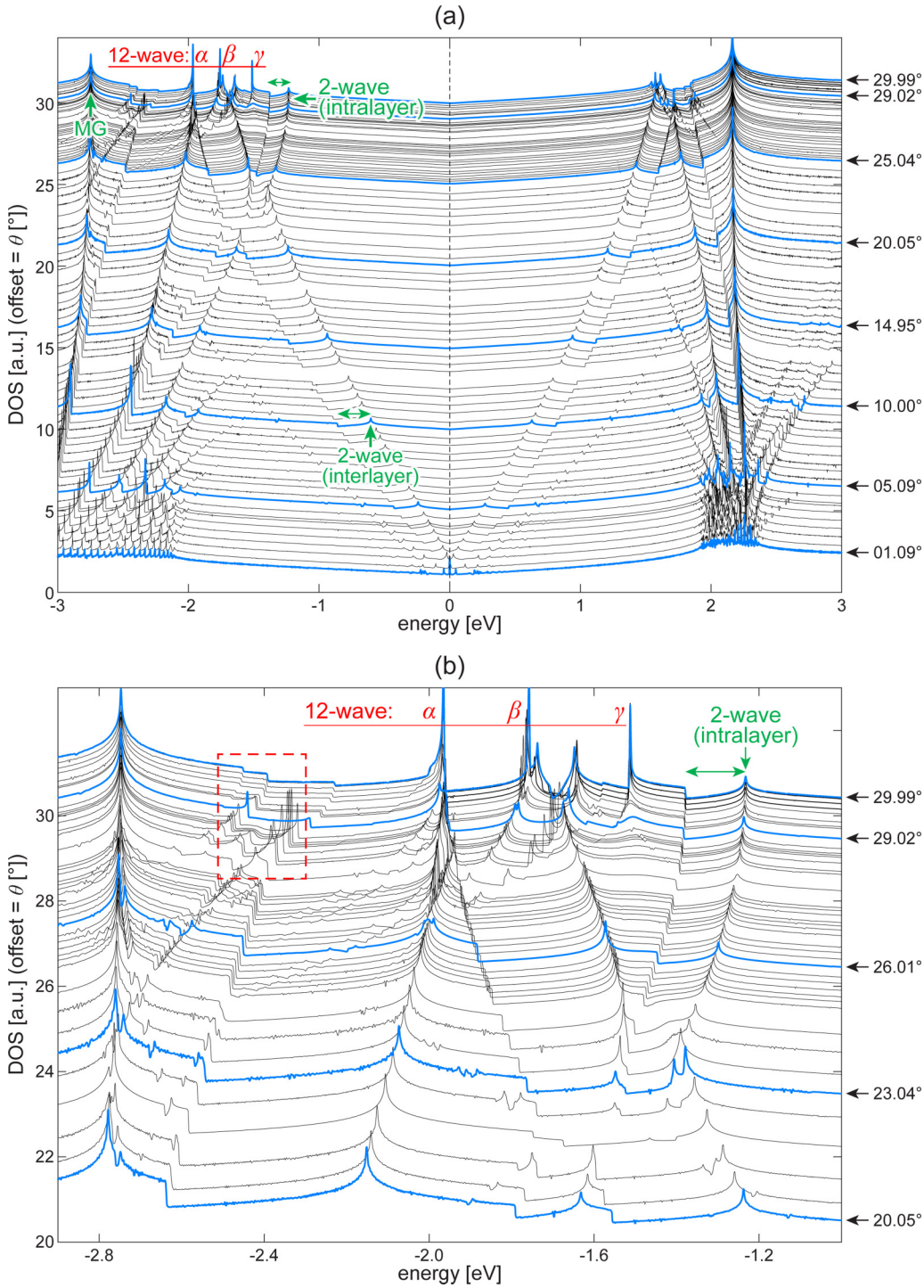

FIG. 8. (a) DOS of TBGs with various rotation angles $0^\circ < \theta < 30^\circ$ in a wide range of energy. Each line is offset along the vertical direction by θ. Peaks marked with green arrows correspond to the van Hove singularity of monolayer graphene, and 2-wave mixing (interlayer and intralayer) of TBGs, respectively. Peaks marked as α, β, γ correspond to the singularities associated with the resonant states of QC-TBG ($\theta = 30^\circ$). (b) Magnified plot of (a) near the energy ranges of the critical states of QC-TBG.

some small errors in the other energies. In Fig. 7, we see that the 182-wave model almost perfectly overlaps with the DOS of very large finite flakes, while the 12-wave model slightly underestimates/overestimates the density of states far from the resonant-state peaks. We confirmed that further increase of k_c does not change the DOS profile.

APPENDIX B: QUASICRYSTAL APPROXIMANTS

In Sec. III A, we compared the quasicrystalline TBG stacked at 30° (QC-TBG) and its periodic approximant at 29.84°. Actually, there exist infinitely many periodic TBGs in any finite region in θ, just like rational numbers in the real number axis. As we will see in the following, the peak

structure in the density of states changes almost continuously in rotating the twist angle θ, and tracing its evolution is useful to get insights on the connection between QC-TBG and the low-angle moiré TBGs, although the computation requires an enormous number of atomic bases (10^3–10^5 atoms).

Here, we calculated the electronic structures of periodic TBGs with various θ using a tight-binding model. Figure 8(a) shows the evolution of the DOS in a wide range of energy, and Fig. 8(b) is the magnified plot near the critical states of QC-TBG. The peaks marked with "MG" correspond to the van Hove singularity of monolayer graphene. Similarly, "2-wave interlayer" represents the singularity that originates from the two-wave mixing between the states in different layers [45], and "2-wave intralayer" is the mixing between the states in the same layer [18,43]. We show the width of the band opening (pseudogap) from 2-wave-interlayer/-intralayer mixing by the green horizontal arrows.

The sharp peaks marked as α, β, γ correspond to the singularities coming from the 12-wave mixing of QC-TBG, which were described as the nearly flat bands in the quasiband picture in Sec. III A. We can see that the singular peaks rapidly grow as θ approaches 30°. The DOS of the TBG with $\theta = 29.99°$, the periodic TBG closest to 30° in this calculation, is consistent with that of QC-TBG [Fig. 2(a)]. It should be noted that, however, the wave functions of the approximants do not obey the quasicrystalline long-range structure with 12-fold rotational symmetry, as argued in Fig. 3(b). We also see that the peak-and-dip structure in the valence band is much wider than in the conduction band, and it is consistent with the analytic argument in the 12-wave ring model [Eq. (9)].

The peaks enclosed by the red box in Fig. 8(b) are associated with the resonant states other than α, β, γ [i.e., the solutions of Eq. (7) other than α, β, γ]. In the 12-wave model, we can also show that corresponding states have flat dispersion in quasiband structure at $\theta \sim 28°$, and exhibit singularities in DOS. As θ approaches 30°, however, the quasiband becomes dispersive [Fig. 2(b)] and the DOS singularities disappear.

[1] E. J. Mele, Phys. Rev. B **81**, 161405(R) (2010).
[2] Y. Fu, E. J. König, J. H. Wilson, Y.-Z. Chou, and J. H. Pixley, arXiv:1809.04604.
[3] J. M. B. Lopes dos Santos, N. M. R. Peres, and A. H. Castro Neto, Phys. Rev. Lett. **99**, 256802 (2007).
[4] G. Trambly de Laissardière, D. Mayou, and L. Magaud, Nano Lett. **10**, 804 (2010).
[5] S. Shallcross, S. Sharma, E. Kandelaki, and O. A. Pankratov, Phys. Rev. B **81**, 165105 (2010).
[6] E. S. Morell, J. D. Correa, P. Vargas, M. Pacheco, and Z. Barticevic, Phys. Rev. B **82**, 121407(R) (2010).
[7] R. Bistritzer and A. H. MacDonald, Proc. Natl. Acad. Sci. **108**, 12233 (2011).
[8] P. Moon and M. Koshino, Phys. Rev. B **85**, 195458 (2012).
[9] G. Trambly de Laissardière, D. Mayou, and L. Magaud, Phys. Rev. B **86**, 125413 (2012).
[10] C. R. Dean, L. Wang, P. Maher, C. Forsythe, F. Ghahari, Y. Gao, J. Katoch, M. Ishigami, P. Moon, M. Koshino, T. Taniguchi, K. Watanabe, K. L. Shepard, J. Hone, and P. Kim, Nature (London) **497**, 598 (2013).
[11] B. Hunt, J. D. Sanchez-Yamagishi, A. F. Young, M. Yankowitz, B. J. LeRoy, K. Watanabe, T. Taniguchi, P. Moon, M. Koshino, P. Jarillo-Herrero, and R. C. Ashoori, Science **340**, 1427 (2013).
[12] L. A. Ponomarenko, R. V. Gorbachev, G. L. Yu, D. C. Elias, R. Jalil, A. A. Patel, A. Mishchenko, A. S. Mayorov, C. R. Woods, J. R. Wallbank, M. Mucha-Kruczynski, B. A. Piot, M. Potemski, I. V. Grigorieva, K. S. Novoselov, F. Guinea, V. I. Fal'Ko, and A. K. Geim, Nature (London) **497**, 594 (2013).
[13] P. Moon and M. Koshino, Phys. Rev. B **90**, 155406 (2014).
[14] E. Koren and U. Duerig, Phys. Rev. B **93**, 201404(R) (2016).
[15] P. Stampfli, Helv. Phys. Acta **59**, 1260 (1986).
[16] S. J. Ahn, P. Moon, T.-H. Kim, H.-W. Kim, H.-C. Shin, E. H. Kim, H. W. Cha, S.-J. Kahng, P. Kim, M. Koshino, Y.-W. Son, C.-W. Yang, and J. R. Ahn, Science **361**, 782 (2018).
[17] Y. Takesaki, K. Kawahara, H. Hibino, S. Okada, M. Tsuji, and H. Ago, Chem. Mater. **28**, 4583 (2016).
[18] W. Yao, E. Wang, C. Bao, Y. Zhang, K. Zhang, K. Bao, C. K. Chan, C. Chen, J. Avila, M. C. Asensio, J. Zhu, and S. Zhou, Proc. Natl. Acad. Sci. **115**, 6928 (2018).
[19] X. D. Chen, W. Xin, W. S. Jiang, Z. B. Liu, Y. S. Chen, and J. G. Tian, Adv. Mater. **28**, 2563 (2016).
[20] D. Wang, G. Chen, C. Li, M. Cheng, W. Yang, S. Wu, G. Xie, J. Zhang, J. Zhao, X. Lu, P. Chen, G. Wang, J. Meng, J. Tang, R. Yang, C. He, D. Liu, D. Shi, K. Watanabe, T. Taniguchi *et al.*, Phys. Rev. Lett. **116**, 126101 (2016).
[21] Y.-H. Choi, D.-H. Lim, J.-H. Jeong, D. Park, K.-S. Jeong, M. Kim, A. Song, H.-S. Chung, K.-B. Chung, Y. Yi, and M.-H. Cho, ACS Appl. Mater. Interfaces **9**, 30786 (2017).
[22] S. Roche, G. T. De Laissardière, and D. Mayou, J. Math. Phys. **38**, 1794 (1997).
[23] Q. Niu and F. Nori, Phys. Rev. Lett. **57**, 2057 (1986).
[24] M. Kohmoto, B. Sutherland, and C. Tang, Phys. Rev. B **35**, 1020 (1987).
[25] K. Niizeki and T. Akamuatsu, J. Phys.: Condens. Matter **2**, 7043 (1990).
[26] J.-M. Gambaudo and P. Vignolo, New J. Phys. **16**, 043013 (2014).
[27] J.-W. Dong, K. H. Fung, C. T. Chan, and H.-Z. Wang, Phys. Rev. B **80**, 155118 (2009).
[28] K. Mnaymneh and R. C. Gauthier, Opt. Express **15**, 5089 (2007).
[29] A. P. Smith and N. W. Ashcroft, Phys. Rev. Lett. **59**, 1365 (1987).
[30] T. Fujiwara and T. Yokokawa, Phys. Rev. Lett. **66**, 333 (1991).
[31] J. Hafner and M. Krajčí, Phys. Rev. Lett. **68**, 2321 (1992).
[32] G. Trambly de Laissardière and T. Fujiwara, Phys. Rev. B **50**, 9843 (1994).
[33] S. Roche and T. Fujiwara, Phys. Rev. B **58**, 11338 (1998).
[34] V. Rogalev, O. Gröning, R. Widmer, J. Dil, F. Bisti, L. Lev, T. Schmitt, and V. Strocov, Nat. Commun. **6**, 8607 (2015).
[35] K. Niizeki, J. Phys. A: Math. Gen. **22**, 193 (1989).

[36] A. I. Goldman and R. F. Kelton, Rev. Mod. Phys. **65**, 213 (1993).
[37] K. Deguchi, S. Matsukawa, N. K. Sato, T. Hattori, K. Ishida, H. Takakura, and T. Ishimasa, Nat. Mater. **11**, 1013 (2012).
[38] J. C. Slater and G. F. Koster, Phys. Rev. **94**, 1498 (1954).
[39] P. Moon and M. Koshino, Phys. Rev. B **88**, 241412(R) (2013).
[40] M. Koshino, New J. Phys. **17**, 015014 (2015).
[41] S. Carr, D. Massatt, M. Luskin, and E. Kaxiras, arXiv:1803.01242.
[42] S. Aubry and G. André, Ann. Isr. Phys. Soc **3**, 18 (1980).
[43] M. Koshino, P. Moon, and Y.-W. Son, Phys. Rev. B **91**, 035405 (2015).
[44] B. L. Chittari, N. Leconte, S. Javvaji, and J. Jung, Electron. Struct. **1**, 015001 (2018).
[45] P. Moon and M. Koshino, Phys. Rev. B **87**, 205404 (2013).